FRONTIERS OF PHYSICS

RESEARCH ARTICLE
Volume 19 / Issue 5 / 53204 / 2024

Multi-terminal pectin/chitosan hybrid electrolyte gated oxide neuromorphic transistor with multi-mode cognitive activities

Yan Li[1,2], You Jie Huang[1], Xin Li Chen[1,2], Wei Sheng Wang[1,2], Xin Huang[1],
Hui Xiao[2], Li Qiang Zhu[1,†]

1 School of Physical Science and Technology, Ningbo University, Ningbo 315211, China
2 Ningbo Institute of Materials Technology and Engineering, Chinese Academy of Sciences, Ningbo 315201, China
Corresponding author. E-mail: †zhuliqiang@nbu.edu.cn

Received January 8, 2024; accepted March 9, 2024

ABSTRACT

In order to fulfill the urgent requirements of functional products, circuit integration of different functional devices are commonly utilized. Thus, issues including production cycle, cost, and circuit crosstalk will get serious. Neuromorphic computing aims to break through the bottle neck of von Neumann architectures. Electronic devices with multi-operation modes, especially neuromorphic devices with multi-mode cognitive activities, would provide interesting solutions. Here, pectin/chitosan hybrid electrolyte gated oxide neuromorphic transistor was fabricated. With extremely strong proton related interfacial electric-double-layer coupling, the device can operate at low voltage of below 1 V. The device can also operate at multi-operation mode, including bottom gate mode, coplanar gate and pseudo-diode mode. Interestingly, the artificial synapse can work at low voltage of only 1 mV, exhibiting extremely low energy consumption of ~7.8 fJ, good signal-to-noise ratio of ~229.6 and sensitivity of ~23.6 dB. Both inhibitory and excitatory synaptic responses were mimicked on the pseudo-diode, demonstrating spike rate dependent plasticity activities. Remarkably, a linear classifier is proposed on the oxide neuromorphic transistor under synaptic metaplasticity mechanism. These results suggest great potentials of the oxide neuromorphic devices with multi-mode cognitive activities in neuromorphic platform.

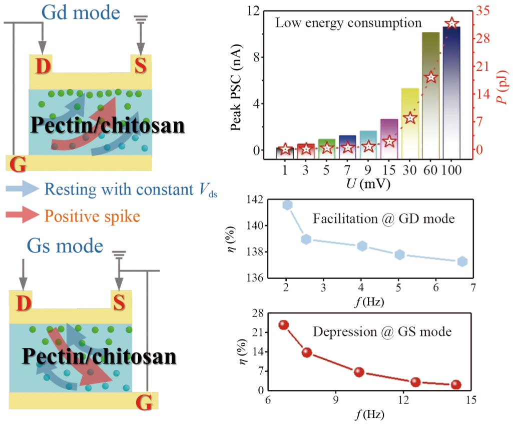

Keywords pectin/chitosan hybrid electrolyte, pseudo-diode function, multi-mode cognitive activities, ultrasensitive oxide neuromorphic device, linear data classifier

1 Introduction

With the arrival of intelligent era, there is a growing need to break away from traditional computer systems with urgent demands for more energy-efficient computing systems [1]. Traditional computing systems rely on Von Neumann architecture, where physical separation of computing units and storage modules results in limited parallel computing and high energy consumption [2]. More importantly, traditional computing systems would get less effective to address the growing demands in machine intelligence. As comparison, after millions of years of evolution and upgrading of the human nervous system, the interconnected neurons form a highly complex neural network structure through synapses with the transmission of electronic and chemical signals [3, 4].

Higher Education Press

https://doi.org/10.1007/s11467-024-1401-z

There are ~10^{11} interconnected neurons in human brain, which can process, respond and store information in an energy-efficient manner [5]. Inspired by the working model of the human nervous system, researchers have been committed to simulating information processing mechanisms in biological nervous system at software and hardware level to achieve autonomous functions and problem solving [6–8]. The implementation of artificial intelligence (AI) algorithms at software level would be fundamentally affected by hardware based devices. Therefore, developments of hardware-based neuromorphic devices are effective ways to implement neuromorphic computing. Since the introduction of the concept of neuromorphic devices in the late 1980s [9], researchers have developed and designed a variety of devices to mimic biological synaptic plasticities. Such neuromorphic devices mainly include two-terminal memristors [10–14] and three-terminal transistors [15–19]. Though two-terminal devices offer several advantages, notably the ability to be highly integrated, the problem of sneak path current leads to a reduction in accurate readout and programming when integrating them into crossed arrays [20]. As comparison, transistor based neuromorphic devices are virtually immune to the "sneak path current" problem due to the fact that transistors operate with gate capacitive coupling mechanism [21]. Thus, three-terminal transistors have also attracted great attention for neuromorphic electronic applications. On the other hand, products with multi-functions are interesting for our daily life. A series of devices with single function could be integrated. However, it would increase the cost of production, the cycle time, and so on. Therefore, multi-mode cognitive activities on single neuromorphic device would endow neuromorphic electronics new intension. Such multi-functional neuromorphic device would have a long-term application prospect.

In the present work, double layered pectin/chitosan composite electrolyte film was adopted to fabricate multi-terminal oxide neuromorphic transistors. The composite film is not only a purely natural biodegradable biomaterial, but also it help to achieve operation with ultra-low power consumption due to the extremely strong proton gating effects. The minimum operating voltage is as low as 1 mV, which is much far below the biological action potential level of ~100 mV [22]. In addition, synaptic plasticities were mimicked on a single oxide neuromorphic transistor with multiple operation modes. With bottom-gate mode, typical synaptic plasticities were mimicked, including excitatory postsynaptic current (EPSC) and paired-pulse facilitation (PPF). Interestingly, linear classification functions were implemented under synaptic metaplasticity mechanisms. With pseudo-diode mode, basic synaptic functions have also been mimicked, including inhibitory/excitatory synaptic responses and spike rate dependent plasticity activities. The composite electrolyte gated oxide neuromorphic transistor can also be degraded in deionized (DI) water, as is in line with the requirements of green sustainable electronics. Here, multiple modes can be achieved on a single environment friendly oxide neuromorphic transistor, exhibiting priorities including low cost, low energy consumption, high sensitivity. As is interesting for the developments of energy-efficient and green AI industry.

2 Experiments

2.1 Fabrication of oxide neuromorphic transistors

Oxide neuromorphic transistors gated with double layered pectin/chitosan composite electrolyte films were fabricated on ITO glass substrates. First, 0.1 g pectin powder (Macklin) was dissolved in 10 mL deionized water. After stirred at 60 °C for 2 h, a homogeneous pectin solution with concentration of ~1.0 wt% was obtained. Chitosan solution was also obtained by dissolving ~0.4 g chitosan powder and ~0.4 g acetic acid in ~20 g deionized waters at room temperature. After standing for 24 h, these solutions can be used. Next, the pectin solution was drop-casted onto the ITO glass substrates. After dried at 40 °C for 12 h, a solid pectin films can be obtained. Then, the chitosan solution was drop-casted on the solid pectin films. After dried at 35 °C for 6 h and followed by drying at 45 °C for 6 h, double layered pectin/chitosan composite electrolyte films were obtained. To obtain oxide transistors, patterned ITO films were sputtered on the double layered electrolyte film by adopting ITO target (In_2O_3: SnO_2 = 90:10 wt%). The sputtering power, working pressure, Ar gas flow rate, and sputtering time were set to 100 W, 0.5 Pa, 14 sccm, and 15 min, respectively. Due to the reflection of ITO nanoparticles at the mask edge, a thin ITO channel can be formed between the source and drain electrodes. Thus, an ITO transistor can be obtained, as schematically shown in Fig. 1(a). The size of the electrodes was 1000 μm × 150 μm. The width and length of the channel layer were 1000 μm and 80 μm, respectively. Interestingly, isolated ITO patterns can also be obtained if they were separated from the source or drain electrodes with a big distances. Such patterns could be deemed as coplanar gates. Such configurations endow the ITO transistors with multi-functions.

2.2 Characterization of double layered pectin/chitosan composite electrolyte films

Surface roughness of the pectin and chitosan films was characterized by using scanning probe microscopy (3100 SPM). Cross-sectional morphology of the double layered pectin/chitosan composite electrolyte films was characterized by scanning electron microscopy. FTIR spectra were analyzed by an intelligent Fourier transform infrared spectrometer (FTIR: Nicolet 6700).

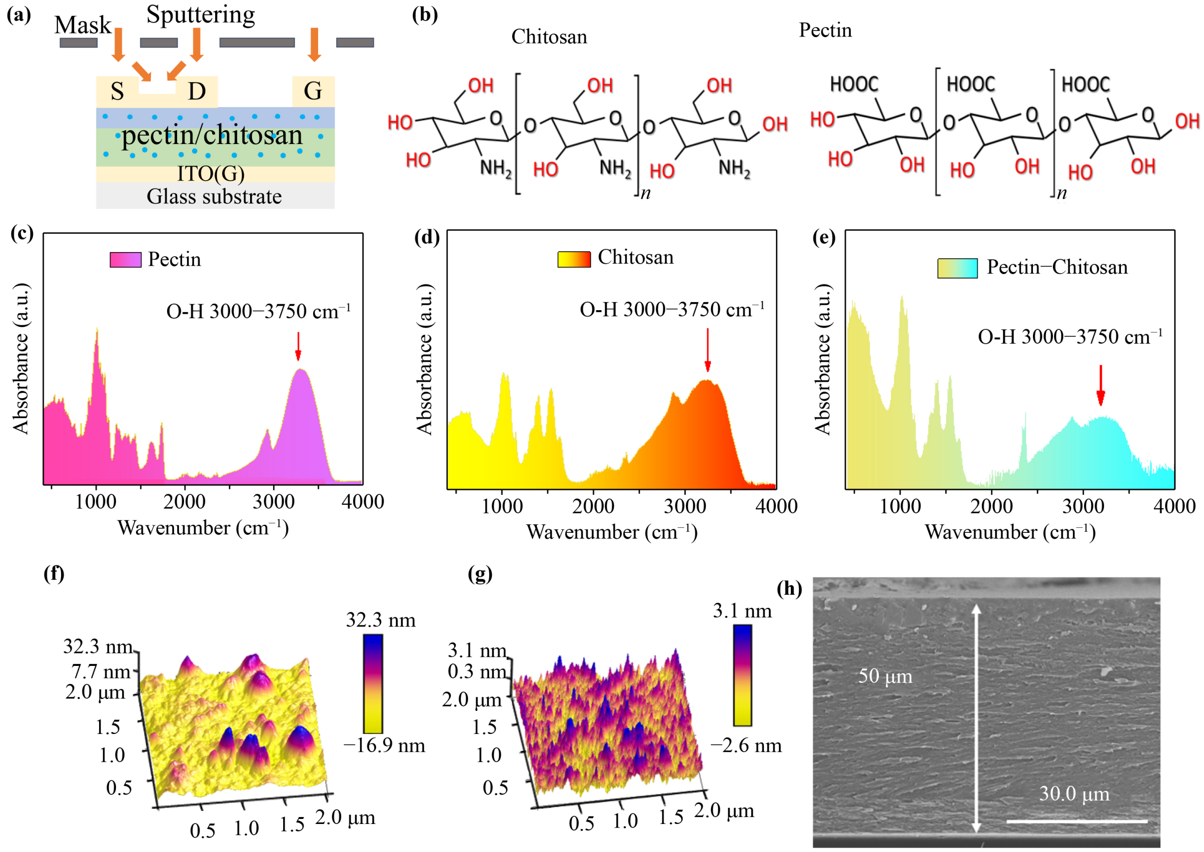

Fig. 1 (**a**) Schematic diagram for depositing of ITO patterns on electrolyte. (**b**) Molecular structures of chitosan and pectin. FTIR spectra of (**c**) pectin, (**d**) chitosan and (**e**) double-layered pectin/chitosan composite electrolyte film. AFM surface topography image of (**f**) pectin film and (**g**) chitosan film. (**h**) Cross-sectional SEM image for the composite electrolyte film.

2.3 Electrical performance characterization

Proton conductivity and frequency-dependent capacitances of the double layered pectin/chitosan composite electrolyte films were characterized by a Solartron1260A Impedance Analyzer. Electrical characteristics of the ITO transistors and multi-mode cognitive activities were measured at room temperature with a semiconductor parameter analyzer (Keithley 4200A SCS). All the electrical characterizations were conducted in atmosphere ambient with air relative humidity of ~60%.

3 Results and discussion

As recyclable renewable resources, pectin and chitosan are widely distributed in nature. Pectin is mainly extracted from fruits, for example, citrus or apple peels. While chitosan can be derived from the crustaceans of marine arthropods, the crustaceans of insects, the cell membranes of fungi and algae, etc. Figure 1(b) shows molecular structures of pectin and chitosan. As natural biodegradable materials, there are plenty of carboxyl groups and hydroxyl groups within their molecular structure, demonstrating potentials in protonic conductive electrolyte. Figures 1(c)–(e) show FTIR spectra of pectin, chitosan and double-layered pectin/chitosan composite electrolyte film. Strong bands at ~1734 cm^{-1} can be attributed to stretching vibration of C=O, clearly demonstrating the existence of a mass of carboxyl within the pectin [23]. Wide peaks ranged between 3000 cm^{-1} and 3750 cm^{-1} correspond to tanti-symmetric pinch-stretch vibration of hydroxyl group [24]. Under the action of external electrical field, a large number of transportable protons (H^+) can be produced, which will help the formation of electric-double-layer (EDL). Here, both the apple pectin solution and chitosan solution exhibits acidity with PH value of ~3.35 and ~3.93, respectively. Compared with neutral solution, the electronic activity of the hydrogen-oxygen bond in the acidic solution will be stronger. As would also be helpful for strong proton conductivity. Figure 1(f) shows atomic force microscope (AFM) surface topography image of pectin film. The surface root mean square (rms) roughness is estimated to be ~6 nm. Figure 1(g) shows AFM surface topography image of chitosan film. The surface

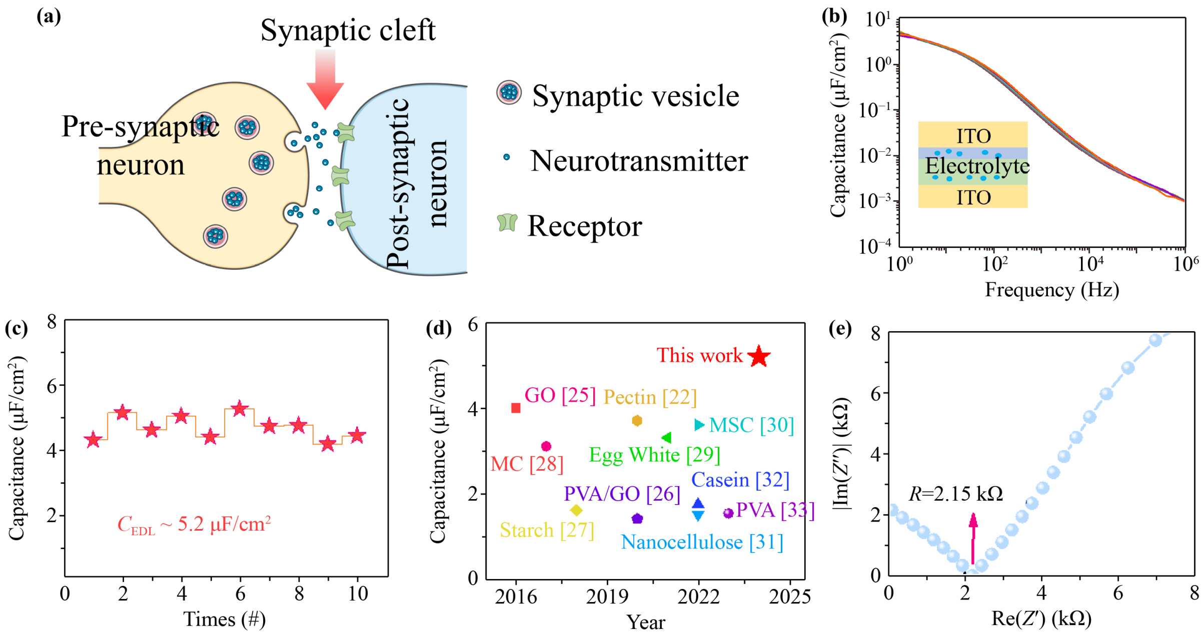

Fig. 2 **(a)** Schematic diagram of a biological synapse. **(b)** Frequency-dependent specific capacitance for double-layered pectin/chitosan composite electrolyte. Inset: ITO/electrolyte/ITO capacitor. **(c)** Extracted EDL capacitances measured for ten times. **(d)** Comparison of the present EDL capacitance with those from the reported works. **(e)** Impedance data of the composite electrolyte film.

rms roughness is estimated to be ~0.8 nm. Since the rms value for chitosan is much lower, it is coated on the pectin to help improve electrical performances. Figure 1(h) shows cross-sectional SEM image for the composite electrolyte film. The thickness is estimated to be ~50 μm. There are also large number of pores. These pores are favorable for proton conductive properties.

Figure 2(a) shows schematic diagram of a biological synapse. When action potential of a presynaptic neuron arrives, the presynaptic membrane releases neurotransmitters from synaptic vesicles. They will diffuse through the synaptic cleft to the postsynaptic membrane and bind to the receptor, triggering post-synaptic responses, i.e., post-synaptic currents and changes in post-synaptic potentials. As a result, information is transmitted from pre-synaptic neuron to post-synaptic neuron. Such synaptic information transferring can be mimicked on the proposed oxide neuromorphic transistor operated in multi-mode. Figure 1(a) schematically shows the double-layered pectin/chitosan composite electrolyte gated ITO neuromorphic transistor. The device can operate at bottom gate mode. When the gate is short connected to the source, it can also operate at pseudo-diode mode. When the lateral ITO pattern is deemed at a gate, the device can also operate at in-plane gate mode. Figure 2(b) shows specific capacitance as a function of frequency. It can be seen that the capacitance presents a strong frequency-dependent characteristics. Figure 2(c) shows the extracted capacitance at 1 Hz measured for ten times. The values are quite stable with average value of ~5.2 μF/cm^2. The results indicate strong stabilities for the present composite electrolyte film. The big specific capacitance is attributed to proton-related EDL effects at the ITO/electrolyte interface. Figure 2(d) compares the EDL capacitance of the present composite electrolyte with those from the reported works [22, 25–33]. It is found that the EDL capacitance of the present composite electrolyte is higher than those from the reported works, indicating the priorities for the present composite electrolyte. Figure 2(e) also shows Cole–Cole plot of impedance data for the composite electrolyte film. The protonic conductivity is estimated to be ~1.57 × 10^{-3} S/cm. It is comparable to or slightly higher than previously reported values for bio-polymer based electrolytes [28–31, 34].

Information transfer between neurons can be simulated on the proposed oxide neuromorphic transistor worked at various operating modes. Firstly, electrical performances have been discussed on the ITO neuromorphic transistor worked at various operating modes. Figure 3(a) is a schematic illustration of an oxide neuromorphic transistor worked at bottom-gate mode (G_B). Figure 3(d) shows ten repeated transfer curves. They overlap with each other very well, indicating good stabilities. Anticlockwise hysteresis are observed, indicating the presence of mobile protons within the composite electrolyte film. V_{ds} is fixed at 1.5 V. Threshold voltage (V_{th}) is estimated to be ~0.1 V. Current on/off ratio is ~4.3 × 10^6. Subthreshold swing is only ~88.7 mV/dec. Carrier mobility is estimated to be ~2.55 cm^2/(V·s). The changes in threshold voltage

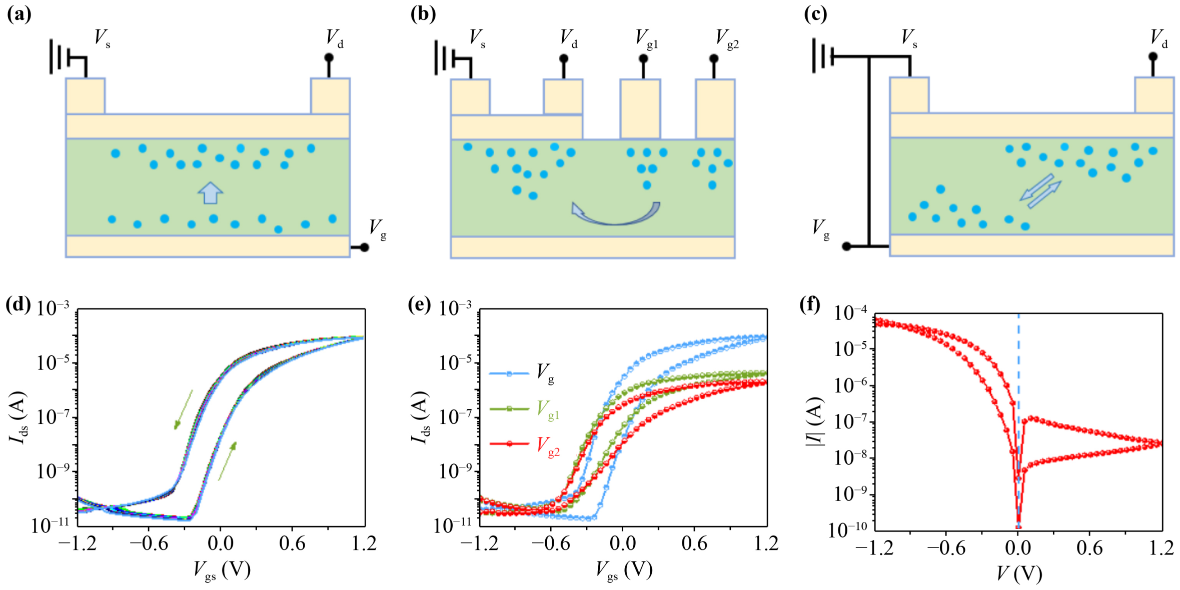

Fig. 3 Schematic illustration of an oxide neuromorphic transistor worked at **(a)** bottom-gate mode (G_B), **(b)** coplanar gate mode and **(c)** pseudo-diode operates at GS mode. **(d)** Transfer curves for G_B mode. **(e)** Comparison of transfer curves for oxide neuromorphic transistor worked at bottom gate mode and coplanar gate mode. **(f)** I–V curve for pseudo-diode operates at GS mode.

(ΔV_{th}) between forward and backward scanning is estimated to be ~0.3 V. Thus, the number of mobile protons can be estimated by using the formula below [35]: $N = \Delta V_{th}\ C/e$, where C and e are the EDL capacitance and the elementary charge, respectively. Thus, the number of the extracted mobile protons is estimated to be ~9.8×10^{12} cm^{-2}. Figure 3(b) is a schematic illustration of an oxide neuromorphic transistor worked at coplanar gate mode. Here, the coplanar gate (G_1) is isolated from the drain electrode for ~300 μm. While at the bottom gate configuration, the distance between the drain and the gate is only ~50 μm. Thus, the gating effects would be a little weaker for the coplanar gate mode. Figure 3(e) compares transfer curves for oxide neuromorphic transistor worked at bottom gate (G_B) mode and coplanar gate mode (V_{G1} or V_{G2}). The on/off ratio for the coplanar gate mode (G_1) is two orders of magnitude lower than that of the bottom gate mode. When the distance between the coplanar gate (G_2) and drain electrode increases to ~690 μm, the gating effects get weak, thus decreasing on/off ratio further. Interestingly, when gate is short connected to source electrode or drain electrode, the neuromorphic transistor could operate at pseudo-diode mode because of the unique proton gating activities. When source is short connected to gate, operation mode is defined as GS mode. While when the drain is short connected to gate, operation mode is defined as GD mode. Here, the bias not only induces current in the diode, but also acts as driving force for the mobile protons within the composite electrolyte film. Figure 3(c) schematically shows pseudo-diode operates at GS mode. The positive bias at the drain will push protons away from the channel/electrolyte interface. Thus, the channel will get depleted and the channel conductivity will decrease. While negative bias will result in the accumulation of protons at the channel/electrolyte interface. Thus, the channel will get accumulated and the channel conductivity will increase. Figure 3(f) shows the I–V curve. The bias is scanned from −1.2 V to 1.2 V and then back. The currents at −1.2 V and 1.2 V are –46.4 μA and 24.4 nA, respectively. Thus, the rectification ratio is estimated to be ~1900.

In order to validate multi-modes of the proposed oxide neuromorphic, pseudo-diode was adopted to mimic synaptic plasticity behavior. Inhibitory synapses and excitatory synapses were mimicked. Different from conventional gate-modulation mode, self-modulation behavior of channel conductance can be achieved only by the drain bias at pseudo-diode mode. Here, synaptic plasticities are mimicked at the GS mode, as schematically shown in Fig. 3(c). Voltage pulses applied on the drain can be considered as pre-synaptic stimuli and the detected drain current can be considered as a post-synaptic current (PSC). Figure 4(a) shows typical PSC response triggered with a pre-synaptic stimulus (1 V, 20 ms) loaded on the drain. When spike comes, a PSC current with peak value of ~0.17 μA is obtained. It is similar to the depolarization process of membrane potential in biological neurons [36]. While within the pre-synaptic spike duration, protons would come to leave electrolyte/channel interface, inducing the decreased channel conductivity. Interestingly, a negative PSC with negative peak value of ~ −33 nA is observed when pre-synaptic spike ends. Such PSC response will gradually decay to

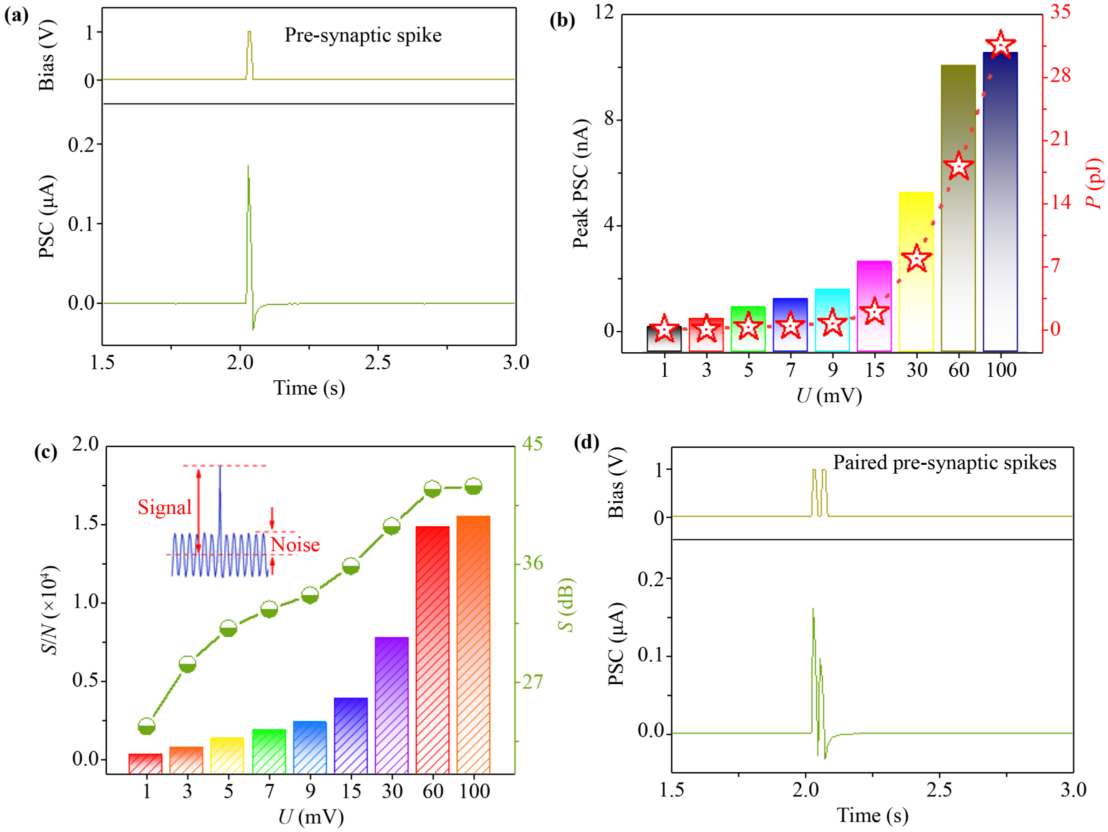

Fig. 4 Typical synaptic responses on GS mode. **(a)** Typical PSC response triggered with a pre-synaptic stimulus (1 V, 20 ms) loaded on the drain. **(b)** Peak PSC values and energy consumption (P) values as a function of spike amplitudes (U). **(c)** S/N and S values as a function of U values. Inset: Schematic diagram for estimate S/N. **(d)** Typical PSC current under paired pre-synaptic spikes.

the resting current. The behavior could be attributed to the relaxation of protons, i.e., the protons migrate back to their initial equilibrium positions. Such PSC response is quite similar to the hyperpolarization process of membrane potential in biological neurons [37].

Additionally, the pseudo-diode mode possesses priorities of ultrasensitive response behaviors, as is highly desirable for energy efficient neuromorphic electronics. Figure 4(b) shows peak PSC values triggered by presynaptic spikes with different spike amplitudes (U). Amplitudes of presynaptic spikes gradually reduced from 100 mV to 1 mV. At the lowest spike amplitude of 1 mV, a peak PSC value of ~0.3 nA is obtained. Here, the energy consumption (P) is also calculated using formula: $P = I_{\text{psc}} \times U \times t$. Figure 4(b) also shows P values as a function of spike amplitudes (U). With the decreased U values, the P values decrease correspondingly. When U is 100 mV, the P value is ~31.5 pJ. While at U of 1 mV, the P value is only ~7.8 fJ. Furthermore, sensitivity is also an important parameter for neuromorphic devices with accurate responses. Here, signal-to-noise ratio (S/N) and sensitivity (S) are investigated at low pre-synaptic amplitude. S value can be obtained with formula: $S = 10\ \log(S/N)$. Figure 4(c) shows S/N and S values as a function of U values. At U value of 100 mV, S/N value and S value are ~15477 and ~41.9 dB, respectively. When the U value decreases to 1 mV, the S/N value is ~229.6. Correspondingly, the S value is as high as ~23.6 dB. The results verify the feasibility of the present pseudo-diode in brain-inspired ultrasensitive neuromorphic devices. With the pseudo-diode mode, short-term synaptic plasticity (STP) can also be mimicked. Figure 4(d) shows PSC current under paired pre-synaptic spikes. Spike duration time, spike interval time and spike amplitude are 10 ms, 20 ms and 1 V, respectively. For the first spike, the peak PSC value (A_1) is ~160.7 nA. While for the second spike, the peak PSC value (A_2) is only ~96.6 nA. The result is quite similar to the paired pulse depression (PPD) behaviors in biological synapses [38, 39]. Here, PPD index (ξ) can be estimated by a formula: $\xi = A_2/A_1 \times 100\%$. Thus, ξ is ~60.1%. The behaviors could be explained as follows. At the short spike interval, some protons induced by the first spike will reside at the electrolyte/gate interface. Upon the arrival of second spike, more protons will get accumulated at the electrolyte/gate interface, leading to a decreased channel conductances, i.e., the decreased peak PSC value for the second spike.

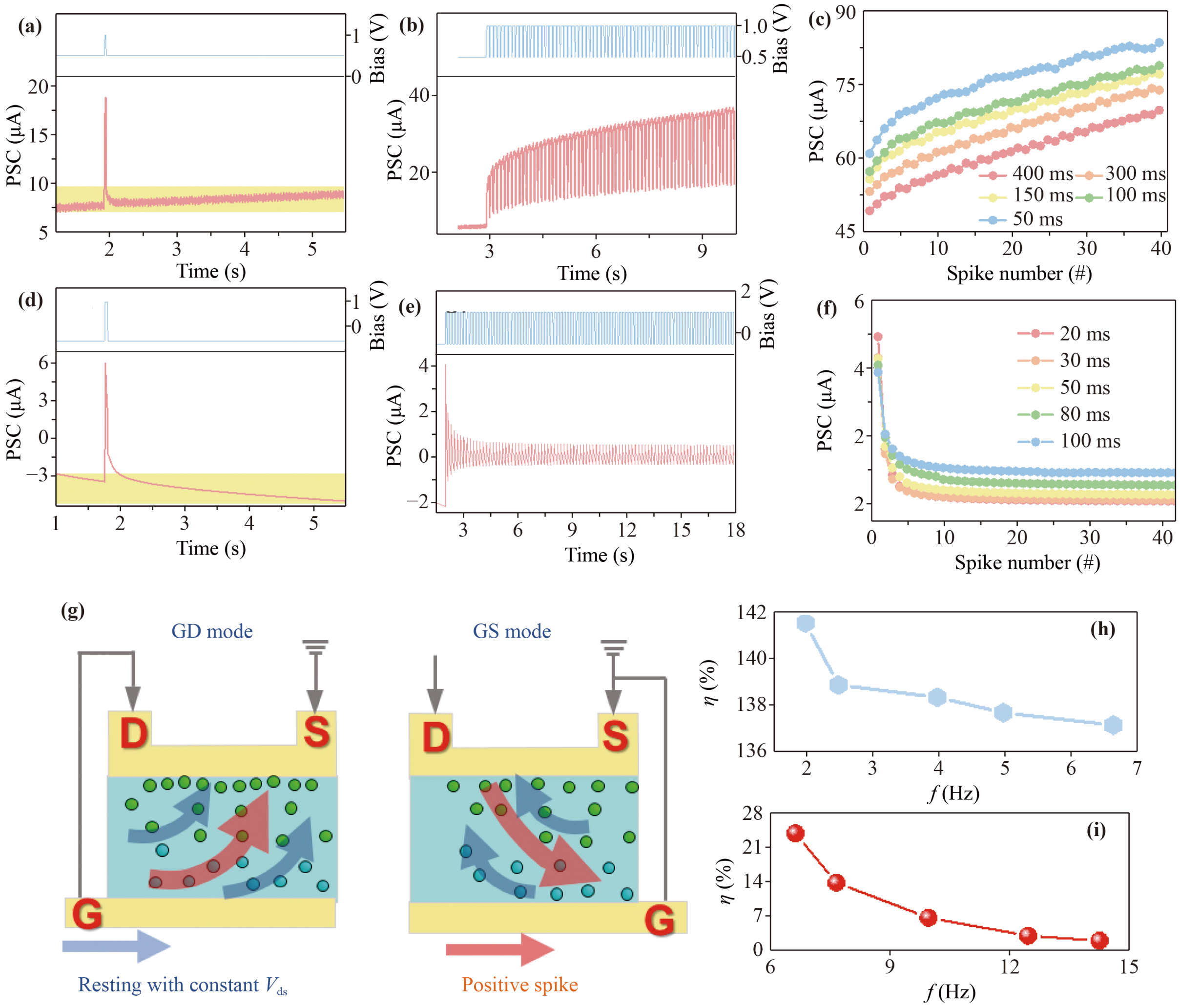

Fig. 5 **(a–c)** Synaptic responses on pseudo-diode with GD mode. (a) Typical PSC response triggered by a pre-synaptic spike (1 V, 30 ms) with a base voltage of 0.5 V. (b) PSC responses with successive spikes of (1 V, 100 ms). Spike interval time (ΔT_{pre}) is 30 ms. (c) Peak PSC value as a function of spike numbers with different ΔT_{pre}. The spike amplitude and spike duration are 1.5 V and 100 ms, respectively. **(d–f)** Synaptic responses on pseudo-diode with GS mode. (d) PSC response triggered by a pre-synaptic spike (1 V, 50 ms) with a base voltage of –0.5 V. (e) PSC responses with successive spikes of (1 V, 100 ms). ΔT_{pre} is 80 ms. (f) Peak PSC value as a function of spike numbers with different ΔT_{pre}. The spike amplitude and duration time are 1 V and 50 ms, respectively. **(g)** Schematic diagram of dynamic proton gating effects on pseudo-diode. **(h)** Frequency dependent facilitation index (η) for GD mode. **(i)** Frequency dependent depression index (η) for GS mode.

The pseudo-diode can also operate at GD mode. Figure 5(a) shows a typical PSC response triggered by a pre-synaptic spike of 1 V in amplitude with a base voltage of 0.5 V. The base voltage induces the accumulation of protons at the electrolyte/channel interface. Thus, a resting drain current of ~8 μA is observed. When pre-synaptic spike of (1 V, 30 ms) arrives, more protons will accumulate at the electrolyte/channel interface, which induces a high peak PSC value of ~18.9 μA. When pre-synaptic spike ends, the accumulated protons will gradually spread out, which results in the decreased channel conductance. Facilitating behavior can also be observed when successive spikes are loaded on the gate. Figure 5(b) shows PSC responses with successive spikes of (1 V, 100 ms). The spike interval time (ΔT_{pre}) is 30 ms. The operation mechanisms are related to the accumulated protons at the electrolyte/channel interface for the increased spike numbers. Figure 5(c) shows peak PSC value as a function of spike numbers with different ΔT_{pre}. When ΔT_{pre} is 400 ms, the peak PSC values increase from ~49.3 μA to ~59.8 μA with spike number increased from 1 to 40. When ΔT_{pre} is 50 ms, the peak PSC values increase from ~60.9 μA to ~83.6 μA with spike number increased from 1 to 40. Similarly, PSC response triggered by a pre-synaptic spike of 1 V in amplitude with a base voltage of –0.5 V is also measured on pseudo-diode operated at GS mode, as shown in Fig. 5(d). The spike duration is 50 ms. With the base voltage of -0.5 V, protons would accumulated at the electrolyte/channel interface, thus a resting current of ~ –3.5 μA can be detected. When a positive pre-synaptic spike arrives, an absolute channel current with peak value of ~6.04 μA is detected. Here, the peak PSC value in GS mode is relatively lower than that in GD mode. The behaviors can be explained below. Dynamic stimuli on the drain will be more effective with the GD mode. In another word, positive spike will load on both gate and drain, which will induces more protons at the electrolyte/channel interface, as schematically shown in the left panel in Fig. 5(g). Thus, the spike will facilitate the channel conductance. While at GS mode, positive spike will result in the decreased proton concentration at the electrolyte/channel interface, as schematically shown in right panel in Fig. 5(g). In another word, the spikes will depress the channel conductance. Figure 5(e) shows the PSC responses with successive spikes of (1 V, 100 ms) at GS mode. The spike interval time is 80 ms. It is observed that the peak PSC value decreases gradually, exhibiting inhibitory behavior. The behavior clearly proves the depression activities. Here, the arrival of drain spike would induce the accumulation of protons at the electrolyte/gate interface. With the increased spike numbers, more and more protons will get accumulated at the electrolyte/gate interface. Figure 5(f) shows the peak PSC value as a function of spike numbers with different interval time ($\Delta T_{\rm pre}$). When $\Delta T_{\rm pre}$ is 100 ms, the peak PSC values decrease from ~3.9 μA to ~0.9 μA with spike number increased from 1 to 40. When $\Delta T_{\rm pre}$ is 20 ms, the peak PSC values decrease from ~4.9 μA to ~92.3 nA with spike number increased from 1 to 40. The two sets of data in Figs. 5(c) and (f) demonstrate that the devices are capable of achieving spike rate-dependent plasticity (SRDP), which is an important synaptic learning function. Here, facilitation index (or depression index) is defined as: $\eta = 100 \times A_{40}/A_1$, where A_{40} and A_1 are the peak PSC values for the 40th spike and 1st spike, respectively. Figures 5(h) and (i) show the frequency dependent η values at GD mode and GS mode, respectively. It is observed that the frequency has significant effects on η values at both the GD mode and the GS mode. In GD mode, the η value is ~141.6% at frequency of 2 Hz, while it decreases to ~137.2% at frequency of 6.7 Hz. In GS mode, the η value also decreases with frequency. It is ~ 23.9% at frequency of 6.7 Hz, while it is ~1.9% at frequency of 14.3 Hz. Though η value decreases with frequency for both modes, it demonstrates facilitation at GD mode, while it demonstrates depression at GS mode. As would be meaningful for the SRDP applications.

We also mimicked basic synaptic plasticities on the ITO neuromorphic transistor with bottom gate configuration. As a typical synaptic feature in biological neural systems, paired-pulse facilitation (PPF) is a kind of short-term synaptic plasticity, reflecting temporal coupling activities. Figure 6(a) illustrates EPSC response triggered by paired pre-synaptic spikes (1 V, 10 ms) with spike interval time (ΔT) of 20 ms. $V_{\rm ds}$ is fixed at 1 V to detect the EPSC response. The first absolute EPSC value (A_1) and the second absolute EPSC value (A_2) are ~2.3 μA and ~2.9 μA, respectively. The PPF index, defined as $\xi = A_2/A_1 \times 100\%$, is ~126%. Figure 6(b) shows ξ values as a function of ΔT. When ΔT is 10 ms, ξ value is ~146%. When ΔT is 800 ms, ξ value drops to ~102%. These behaviors are quite similar to the PPF response in biological synapses. Here, the ξ vs. ΔT curve is also fitted with a dual-phase exponential function [40]:

$$\xi = 1 + C_1 \times {\rm e}^{-\Delta T/\tau_1} + C_2 \times {\rm e}^{-\Delta T/\tau_2},$$

where C_1 and C_2 are the initial facilitation parameters, while τ_1 and τ_2 are the characteristic relaxation times. C_1, C_2, τ_1 and τ_2 are estimated to be ~9.42%, ~112.94%, ~312 ms and ~18 ms, respectively. These values are quite similar to those in biological synapses. In neural system, historical stimuli often affects synaptic plasticity and cognitive activities. The behavior is called as synaptic metaplasticity. [41] With the inherent priorities for proton gating, historical stimuli would affect the synaptic responses on the followed pre-synaptic spikes independent of operation mode. Thus, metaplasticity could be mimicked on different operation modes. Here, metaplasticity is mimicked on the bottom gate mode. Figure 6(c) schematically shows the spiking trains consisted of priming spike and main spike on the gate. The main spike duration time is 10 ms. To detect EPSC responses, a constant $V_{\rm ds}$ of 0.5 V is loaded. Figure 6(d) shows EPSC responses with the increased priming spike duration time. The spike interval time (ΔT) is fixed at 50 ms. With the increased duration times of the priming spike from 20 ms to 1980 ms, there is a significant increase in the EPSC value from ~0.3 μA to ~1.0 μA. This indicates that the height of the main spike can be modulated by the duration time of the priming spike. Figure 6(e) shows the EPSC responses with the increased ΔT. The duration time of the priming spike is fixed at 1980 ms. It is observed that the main peak EPSC value decrease gradually from 1.1 μA to 0.6 μA with the increased ΔT from 20 ms to 500 ms. Such synaptic metaplasticity hints that information of the historical priming spikes can be judged by reading the EPSC responses at the main spike. Here, the oxide neuromorphic transistor is proposed as a linear classifier capable of classifying processing. As shown in Fig. 6(c), the priming spike can be deemed as the input information. Main spike of 0.5 V in amplitude and of 10 ms in duration is deemed as a reading spike. Thus, main EPSC response contains input information and can be used for realizing classification function. Figure 6(f) shows the gradient plot with different priming spike duration and spike ΔT. Here, a threshold

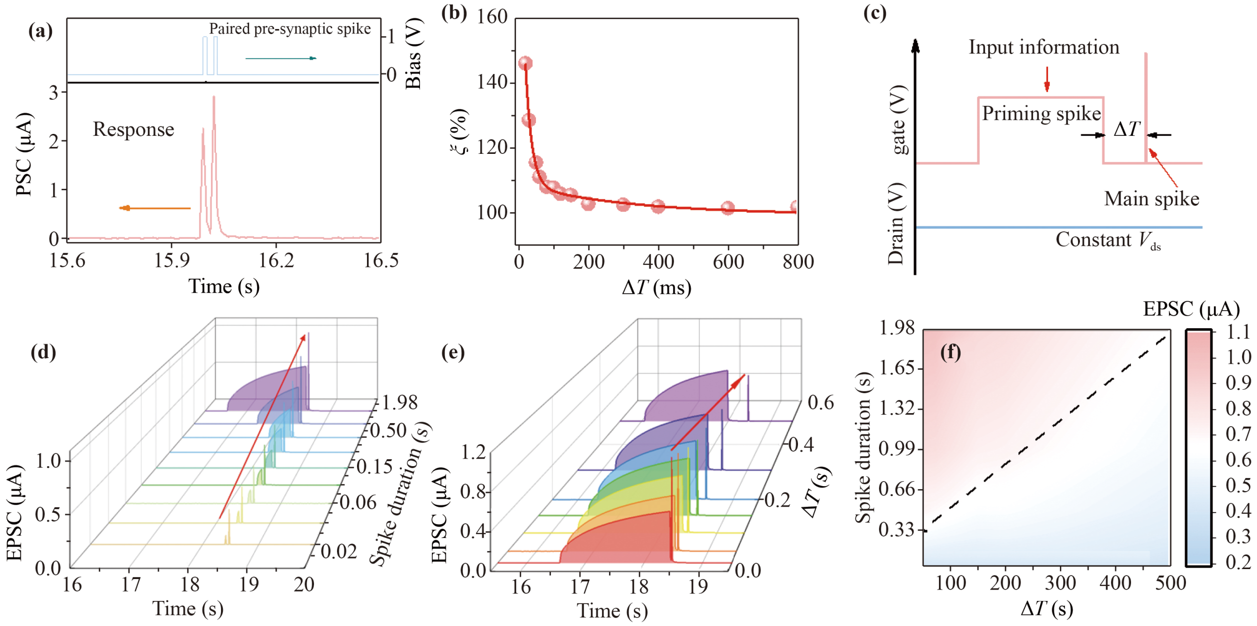

Fig. 6 **(a)** EPSC response on oxide neuromorphic transistor triggered with paired pre-synaptic spikes (1 V, 10 ms) with spike interval time (ΔT) of 20 ms. **(b)** PPF index (ξ) as a function of ΔT. **(c)** Schematically diagram of the spiking trains consisted of priming spike and main spike. **(d)** EPSC responses with the increased priming spike duration time. ΔT is fixed at 50 ms. **(e)** EPSC responses with the increased ΔT. The duration time of the priming spike is fixed at 1980 ms. **(f)** Gradient plot with different priming spike duration and spike ΔT.

value of 0.64 μA is set. When peak value is above 0.64 μA, the output data is located at the up left corner of the classification field, which implies that the input is either close to the main spike or the input is more informative, i.e., big spike duration. In contrast, when peak value is below 0.64 μA, the output data is located at the right lower corner of the classification field, which implies that the input is away from the main spike or the input is less informative, i.e., short spike duration. The integrated output function implies that the oxide neuromorphic transistors have good co-modulation with information processing and have the ability to realize linear classification function on a single oxide neuromorphic transistor. These conclusions point to the fact that the oxide neuromorphic transistors have potentials in simplifying cognitive neuromorphic platforms.

4 Conclusion

In summary, multi-functional oxide neuromorphic transistor were fabricated with a single-step mask processing. The devices were gated with pectin/chitosan hybrid electrolyte. Due to the extremely strong interfacial ionic/electronic coupling effect, the oxide neuromorphic transistor can operate at low voltage below 1 V. With unique protonic gating and drain self-modulation, the device can also operate at multi-operation mode, including bottom gate mode, coplanar gate and pseudo-diode mode. Interestingly, the artificial synapse can work at low voltage of only 1 mV, exhibiting extremely low energy consumption of ~7.8 fJ, good signal-to-noise ratio of ~229.6 and sensitivity of ~23.6 dB. Both inhibitory and excitatory synaptic responses were mimicked on the pseudo-diode with GS mode and GD mode, respectively. Moreover, spike rate dependent plasticity activities were observed. With synaptic metaplasticity activities for the oxide neuromorphic transistor under bottom gate configuration, a linear classifier is proposed, exhibiting interesting classification function. These results suggest great potentials of the oxide neuromorphic devices with multi-mode cognitive activities in neuromorphic platform.

Declarations The authors declare that they have no competing interests and there are no conflicts.

Acknowledgements This work was supported by the National Natural Science Foundation of China (Nos. 51972316 and U22A2075) and Ningbo Key Scientific and Technological Project (No. 2021Z116).

References

1. J. Backus, Can programming be liberated from the von Neumann style? A function style and its algebra of programs *Commun. ACM* 21(8), 613 (1978)
2. M. D. Godfrey and D. F. Hendry, The computer as von Neumann planned it, *IEEE Ann. Hist. Comput.* 15(1), 11 (1993)
3. R. Colom, S. Karama, R. E. Jung, and R. J. Haier,

Human intelligence and brain networks, *Dialogues Clin. Neurosci.* 12(4), 489 (2010)

4. D. F. Lohman, Human intelligence: An introduction to advances in theory and research, *Rev. Educ. Res.* 59(4), 333 (1989)
5. L. F. Abbott and W. G. Regehr, Synaptic computation, *Nature* 431(7010), 796 (2004)
6. E. J. Fuller, S. T. Keene, A. Melianas, Z. R. Wang, S. Agarwal, Y. Y. Li, Y. Tuchman, C. D. James, M. J. Marinella, J. J. Yang, A. Salleo, and A. A. Talin, Parallel programming of an ionic floating-gate memory array for scalable neuromorphic computing, *Science* 364(6440), 570 (2019)
7. M. M. Poo, J. L. Du, N. Y. Ip, Z. Q. Xiong, B. Xu, and T. Tan, China brain project: Basic neuroscience, brain diseases, and brain-inspired computing, *Neuron* 92(3), 591 (2016)
8. M. A. Zidan, J. P. Strachan, and W. D. Lu, The future of electronics based on memristive systems, *Nat. Electron.* 1(1), 22 (2018)
9. C. Mead, Neuromorphic electronic systems, *Proc. IEEE* 78(10), 1629 (1990)
10. M. K. Kim and J. S. Lee, Short-term plasticity and long-term potentiation in artificial biosynapses with diffusive dynamics, *ACS Nano* 12(2), 1680 (2018)
11. J. B. Chen, T. T. Guo, C. Y. Yang, J. W. Xu, L. Y. Gao, S. J. Jia, P. Zhang, J. T. Chen, Y. Zhao, J. Wang, X. Q. Zhang, and Y. Li, Synaptic plasticity of a microfluidic memristor with a temporary memory function based on an ionic liquid in a capillary tube, *J. Phys. Chem. C* 127(6), 3307 (2023)
12. S. H. Jo, T. Chang, I. Ebong, B. B. Bhadviya, P. Mazumder, and W. Lu, Nanoscale memristor device as synapse in neuromorphic systems, *Nano Lett.* 10(4), 1297 (2010)
13. H. Chen, X. G. Tang, Z. H. Shen, W. T. Guo, Q. J. Sun, Z. H. Tang, and Y. P. Jiang, Emerging memristors and applications in reservoir computing, *Front. Phys.* 19(1), 13401 (2024)
14. S. X. Liu, J. M. Zeng, Q. L. Chen, and G. Liu, Recent advances in halide perovskite memristors: From materials to applications, *Front. Phys.* 19(2), 23501 (2024)
15. L. Q. Zhu, C. J. Wan, L. Q. Guo, Y. Shi, and Q. Wan, Artificial synapse network on inorganic proton conductor for neuromorphic systems, *Nat. Commun.* 5(1), 3158 (2014)
16. C. Ge, C. X. Liu, Q. L. Zhou, Q. H. Zhang, J. Y. Du, J. K. Li, C. Wang, L. Gu, G. Z. Yang, and K. J. Jin, A ferrite synaptic transistor with topotactic transformation, *Adv. Mater.* 31(19), 1900379 (2019)
17. H. L. Park, H. Kim, D. Lim, H. Zhou, Y. H. Kim, Y. Lee, S. Park, and T. W. Lee, Retina-inspired carbon nitride-based photonic synapses for selective detection of UV light, *Adv. Mater.* 32(11), 1906899 (2020)
18. Y. B. Guo and L. Q. Zhu, Recent progress in optoelectronic neuromorphic devices, *Chin. Phys. B* 29(7), 078502 (2020)
19. Y. C. Cai, J. Yang, F. Wang, S. H. Li, Y. R. Wang, X. Y. Zhan, F. M. Wang, R. Q. Cheng, Z. X. Wang, and J. He, Ultrasensitive solar-blind ultraviolet detection and optoelectronic neuromorphic computing using α-In_2Se_3 phototransistors, *Front. Phys.* 18(3), 33308 (2023)
20. Q. Xia and J. J. Yang, Memristive crossbar arrays for brain-inspired computing, *Nat. Mater.* 18(4), 309 (2019)
21. S. H. Kim, K. Hong, W. Xie, K. H. Lee, S. Zhang, T. P. Lodge, and C. D. Frisbie, Electrolyte-gated transistors for organic and printed electronics, *Adv. Mater.* 25(13), 1822 (2013)
22. Y. Li, C. Zhang, X. L. Zhao, Y. H. Tong, Q. X. Tang, and Y. C. Liu, Ultrasensitive and degradable ultra-flexible synaptic transistors based on natural pectin, *ACS Appl. Electron. Mater.* 4(1), 316 (2022)
23. R. W. Stoddart, A. J. Barrett, and D. H. Northcote, Pectic polysaccharides of growing plant tissues, *Biochem. J.* 102(1), 194 (1967)
24. T. Weymuth, C. R. Jacob, and M. Reiher, A local-mode model for understanding the dependence of the extended amide III vibrations on protein secondary structure, *J. Phys. Chem. B* 114(32), 10649 (2010)
25. C. J. Wan, Y. H. Liu, P. Feng, W. Wang, L. Q. Zhu, Z. P. Liu, Y. Shi, and Q. Wan, Flexible metal oxide/graphene oxide hybrid neuromorphic transistors on flexible conducting graphene substrates, *Adv. Mater.* 28(28), 5878 (2016)
26. H. Han, L. Q. Zhu, Z. Y. Ren, H. Xiao, and L. Q. Guo, Poly (vinyl alcohol)/graphene oxide hybrid electrolyte gated oxide neuron transistors for multifunctional logic applications, *J. Phys. D Appl. Phys.* 53(11), 115106 (2020)
27. L. Q. Guo, J. Tao, L. Q. Zhu, H. Xiao, W. T. Gao, F. Yu, and Y. M. Fu, Starch-based biopolymer electrolyte gated oxide synaptic transistors, *Org. Electron.* 61, 312 (2018)
28. C. J. Wan, L. Q. Zhu, X. Wan, Y. Shi, and Q. Wan, Organic/inorganic hybrid synaptic transistors gated by proton conducting methylcellulose films, *Appl. Phys. Lett.* 108(4), 043508 (2016)
29. Z. Y. Li, L. Q. Zhu, L. Q. Guo, Z. Y. Ren, H. Xiao, and J. C. Cai, Mimicking neurotransmitter activity and realizing algebraic arithmetic on flexible protein-gated oxide neuromorphic transistors, *ACS Appl. Mater. Interfaces* 13(6), 7784 (2021)
30. Z. Y. Ren, Y. H. Kong, L. Ai, H. Xiao, W. S. Wang, Z. W. Shi, and L. Q. Zhu, Proton gated oxide neuromorphic transistors with bionic vision enhancement and information decoding, *J. Mater. Chem. C* 10(18), 7241 (2022)
31. W. S. Wang, Z. W. Shi, X. L. Chen, Y. Li, H. Xiao, Y. H. Zeng, X. D. Pi, and L. Q. Zhu, Biodegradable oxide neuromorphic transistors for neuromorphic computing and anxiety disorder emulation, *ACS Appl. Mater. Interfaces* 15(40), 47640 (2023)
32. H. S. Kim, H. Park, and W. J. Cho, Biocompatible casein electrolyte-based electric-double-layer for artificial synaptic transistors, *Nanomaterials (Basel)* 12(15), 2596 (2022)
33. D. H. Lee, H. Park, and W. J. Cho, Synaptic transistors based on PVA: Chitosan biopolymer blended electric-double-layer with high ionic conductivity, *Polymers (Basel)* 15(4), 896 (2023)
34. T. Y. Long, L. Q. Zhu, Z. Y. Ren, and Y. B. Guo, Global modulatory heterosynaptic mechanisms in biopolymer electrolyte gated oxide neuron transistors, *J.*

Phys. D Appl. Phys. 53(43), 435105 (2020)

35. W. Dou, W. Hou, Y. Y. Tan, X. M. Gan, Z. R. Xie, X. Yuan, L. H. Lei, and J. L. Zhang, Flexible transparent electric-double-layer junctionless thin film transistors with low operating voltage, *ECS J. Solid State Sci. Technol.* 10(11), 115003 (2021)
36. S. Ghoshal and J. Claassen, Spreading depolarization and acute ischaemia in subarachnoid haemorrhage: the role of mass depolarization waves, *Brain* 140(10), 2527 (2017)
37. W. Li, C. X. Wu, J. W. Hou, J. Sun, Q. S. Wang, P. P. Zhang, Y. Yu, M. Yang, M. Chen, B. F. Mo, Y. P. Wang, and Y. G. Li, Higher sodium channel excitability in cardiac purkinje fibers: Implications for multifocal ectopic purkinje-related premature contractions, *JACC Clin. Electrophysiol.* 9(12), 2477 (2023)
38. D. Debanne, N. C. Guerineau, B. H. Gahwiler, and S. M. Thompson, Paired pulse facilitation and depression at unitary synapses in rat hippocampus quantal fluctuation affects subsequent release, *J. Physiol.* 491(1), 163 (1996)
39. R. F. Waldeck, A. Pereda, and D. S. Faber, Properties and plasticity of paired- pulse depression at a central synapse, *J. Neurosci.* 20(14), 5312 (2000)
40. M. A. Mukhamedyarov, S. N. Grishin, A. L. Zefirov, and A. Palotas, The mechanisms of multi-component paired-pulse facilitation of neurotransmitter release at the frog neuromuscular junction, *Pflugers Arch.* 458(3), 563 (2009)
41. I. Sotiropoulos and J. L. Trejo, Brain metaplasticity, *Neuroscience* 454, 1 (2021)